Reaction-Induced Metal-Metal Oxide Interactions in Pd-In$_2$O$_3$/ZrO$_2$ Catalysts Drive Selective and Stable CO$_2$ Hydrogenation to Methanol

Journal Article

Author(s):
Pinheiro Araújo, Thaylan; Morales-Vidal, Jordi; Giannakakis, Georgios (ID); Mondelli, Cecilia; Eliasson, Henrik; Erni, Rolf (ID);
Stewart, Joseph A.; Mitchell, Sharon; López, Núria; Pérez-Ramírez, Javier

GDCh

Research Articles

Angewandte
Chemie
International Edition
www.angewandte.org

Heterogeneous Catalysis

Reaction-Induced Metal-Metal Oxide Interactions in Pd-In$_2$O$_3$/ZrO$_2$ Catalysts Drive Selective and Stable CO$_2$ Hydrogenation to Methanol

Thaylan Pinheiro Araújo[+], Jordi Morales-Vidal[+], Georgios Giannakakis, Cecilia Mondelli, Henrik Eliasson, Rolf Erni, Joseph A. Stewart, Sharon Mitchell, Núria López, and Javier Pérez-Ramírez

Abstract: Ternary Pd-In$_2$O$_3$/ZrO$_2$ catalysts exhibit technological potential for CO$_2$-based methanol synthesis, but developing scalable systems and comprehending complex dynamic behaviors of the active phase, promoter, and carrier are key for achieving high productivity. Here, we show that the structure of Pd-In$_2$O$_3$/ZrO$_2$ systems prepared by wet impregnation evolves under CO$_2$ hydrogenation conditions into a selective and stable architecture, independent of the order of addition of Pd and In phases on the zirconia carrier. Detailed *operando* characterization and simulations reveal a rapid restructuring driven by the metal-metal oxide interaction energetics. The proximity of InPd$_x$ alloy particles decorated by InO$_x$ layers in the resulting architecture prevents performance losses associated with Pd sintering. The findings highlight the crucial role of reaction-induced restructuring in complex CO$_2$ hydrogenation catalysts and offer insights into the optimal integration of acid-base and redox functions for practical implementation.

Introduction

In 2016, indium oxide (In$_2$O$_3$) was identified as a highly selective catalyst for methanol synthesis via carbon dioxide hydrogenation (CO$_2$ + 3H$_2$ ⇌ CH$_3$OH + H$_2$O), a sustainable route to produce this vital commodity and energy carrier.[1–3] Detailed mechanistic studies showed that surface oxygen vacancies formed upon reaction are key to creating a catalytic ensemble that favors methanol formation while suppressing undesired carbon monoxide production through the reverse water-gas shift reaction (RWGS, CO$_2$ + H$_2$ ⇌ CO + H$_2$O).[4] Nonetheless, methanol space-time yield (*STY*) over In$_2$O$_3$ is limited and therefore many efforts have since been devoted to enhance its overall catalytic performance.[5–15] Two effective strategies towards this goal comprise deposition on *monoclinic* zirconia (*m*-ZrO$_2$) and palladium promotion as both approaches boost oxygen vacancy generation and also, in the case of the latter, enhances H$_2$ splitting, which limits the rate of unmodified In$_2$O$_3$.[1,5,7,8,13] Additionally, the *m*-ZrO$_2$ support grants improved CO$_2$ adsorption capacity and indium dispersion.[1,13,14,16] Integrating both strategies via flame spray pyrolysis (FSP) yielded a ternary Pd-In$_2$O$_3$/ZrO$_2$ catalyst demonstrating *ca.* 2 to 3-fold higher methanol productivity than that of binary counterparts (1 wt % Pd/In$_2$O$_3$ and 5 wt % In$_2$O$_3$/ZrO$_2$), and thus realistic prospects for practical application.[17]

While this example demonstrates the potential of Pd-In$_2$O$_3$/ZrO$_2$ catalysts for CO$_2$ hydrogenation, catalytic materials synthesized by FSP generally exhibit unique structures and properties compared to those obtained by commonly practiced wet-chemistry routes, due to intrinsic steps involved in FSP synthesis such as exposure to high temperatures (*i.e.*, 2000-3000 K) and rapid quenching.[18–20] Consequently, our understanding of the catalyst architecture and associated reactivity of Pd-In$_2$O$_3$/ZrO$_2$ systems synthesized by scalable routes such as impregnation remains limited. Additionally, multicomponent catalysts often experience

[*] T. P. Araújo,[+] Dr. G. Giannakakis, Dr. C. Mondelli, Dr. S. Mitchell, Prof. J. Pérez-Ramírez
Institute of Chemical and Bioengineering, Department of Chemistry and Applied Biosciences, ETH Zurich
Vladimir-Prelog-Weg 1, 8093 Zurich (Switzerland)
E-mail: jpr@chem.ethz.ch

J. Morales-Vidal,[+] Prof. N. López
Institute of Chemical Research of Catalonia (ICIQ-CERCA), The Barcelona Institute of Science and Technology
Av. Països Catalans 16, 43007 Tarragona (Spain)

J. Morales-Vidal[+]
Universitat Rovira i Virgili
Av. Catalunya 35, 43002 Tarragona (Spain)

H. Eliasson, Prof. R. Erni
Electron Microscopy Center, Empa, Swiss Federal Laboratories for Materials Science and Technology
Überlandstrasse 129, 8600 Dübendorf (Switzerland)

Dr. J. A. Stewart
TotalEnergies OneTech Belgium
Zone Industrielle Feluy C, 7181 Seneffe (Belgium)

[+] These authors contributed equally to this work.

surface reconstruction in response to reactive environments, which directly impacts their catalytic response.[16,21–23] Various phenomena have been reported for Pd/In_2O_3 catalysts attained by impregnation, such as palladium sintering, formation of palladium-indium intermetallic compounds, and encapsulation of metallic nanoparticles by InO_x overlayers have been reported, leading to diverse outcomes in methanol selectivity.[5,10,11] Moreover, while In_2O_3/m-ZrO_2 systems display stable performance, subnanometric supported In_2O_3 islands or clusters present in the fresh catalysts were substantially altered after the reaction. Besides, no phase intermixing in the form of a solid solution was observed.[24] Based on these observations, it is therefore fundamental to understand the structural evolution of Pd-In_2O_3/ZrO_2 catalysts to map the resulting architecture to its function under reaction conditions.

In this study, we uncover that Pd-In_2O_3/ZrO_2 catalysts prepared by impregnation evolve into a unique catalyst architecture under CO_2 hydrogenation, resulting in high methanol selectivity and stable performance. Detailed space and time-resolved analyses using microscopy and *operando* X-ray diffraction (XRD) and X-ray absorption spectroscopy (XAS) reveal that the restructuring process occurs rapidly and is governed by the energetics of metal-metal oxide interactions between each component phase. In essence, partially reduced indium oxide species, InO_x, migrate from the ZrO_2 surface onto palladium nanoparticles (*ca.* 10 nm) present from the catalyst synthesis, inducing the formation of $InPd_x$ alloy domains decorated by InO_x layers. Density functional theory (DFT) simulations indicate that the dynamic behavior of In_2O_3 is directed by its degree of reduction, with InO_x preferably stabilizing over metallic palladium. Remarkably, although palladium exists as nanoparticles, which is well documented to favor CO formation[5,7,11,25,26], this is curtailed on $InPd_x$, which activates H_2 homolytically and its proximity to InO_x is identified as essential for promoting methanol formation. Overall, this study provides atomic-level understanding of the working state of a prospective industrial catalyst for CO_2-based methanol synthesis, highlighting that surface reconstruction and *operando* characterization are critical in advancing the design of practically relevant catalytic materials.

Results and Discussion

Catalytic Performance

Ternary catalysts with optimal nominal contents of In_2O_3 (5 wt%) and palladium (1 wt%)[5,13,17] were prepared by *one* or *two-step* impregnation approaches onto m-ZrO_2 to produce $1Pd$-$5In_2O_3/m$-ZrO_2 and $1Pd/5In_2O_3/m$-ZrO_2, respectively (see full description in the **Experimental Section**, Supporting Information). Binary systems ($1Pd/In_2O_3$, $5In_2O_3/m$-ZrO_2, and $1Pd/m$-ZrO_2) were also synthesized by impregnation for reference (Table S1). All catalysts possessed similar specific surface area (S_{BET}) and nominal In_2O_3 and palladium contents closely matched experimental values (Table S2 and S3). Performance assessment at relevant CO_2

hydrogenation to methanol conditions (5 MPa, 553 K, $H_2/CO_2=4$, and gas-hourly space velocity ($GHSV=24,000\ cm^3\,h^{-1}\,g_{cat}^{-1}$) revealed that both ternary catalysts display very similar methanol space-time yield ($STY=$ *ca.* $0.62\ g_{MeOH}\,h^{-1}\,g_{cat}^{-1}$), which remains unaltered after 50 h on stream and significantly outperforms that of binary counterparts (Figure 1a). The superior methanol productivity of the ternary catalysts is linked to their higher activity in converting CO_2 (Figure S1a). In addition, comparing methanol selectivity (S_{MeOH}, Figure 1b) at similar CO_2 conversion levels ($X_{CO2}=ca.\ 4\%$) showed that these materials are generally more selective than $5In_2O_3/m$-ZrO_2 and especially $1Pd/m$-ZrO_2 ($S_{MeOH}=ca.\ 80\%$ versus 25%). Interestingly, while ternary catalysts and $5In_2O_3/m$-ZrO_2 are remarkably stable, the STY of $1Pd/In_2O_3$ and especially $1Pd/m$-ZrO_2 drops significantly during the first 20 h on stream before stabilizing (Figure 1a). This could be attributed to a moderate decrease in S_{MeOH} (from 80% to 70%, Figure S1b) and losses in both S_{MeOH} (Figure S1b) and particularly X_{CO2} (from 12% to 4%, Figure S1a) for $1Pd/In_2O_3$ and $1Pd/m$-ZrO_2, respectively. In particular, the loss in performance is closely linked to the S_{BET} of these catalysts drastically diminishing (*ca.* 40%, Table S3) upon reaction, hinting at palladium and/or indium oxide sintering, while it remained virtually unchanged for ternary systems and $5In_2O_3/m$-ZrO_2. Analysis by scanning transmission electron microscopy coupled to energy-dispersive X-ray spectroscopy (STEM-EDX, Figures S3a,b) revealed that palladium clusters present on fresh $1Pd/m$-ZrO_2 sinter into large nanoparticles (*ca.* 10 nm) with progressing time on stream. For $1Pd/In_2O_3$, considerable agglomeration of palladium into nanoparticles (Figures S5a,b) and In_2O_3 (from 13 to 22 nm as determined by XRD, Figure S2) is observed. In contrast, In_2O_3 is equally well dispersed in fresh and used $5In_2O_3/m$-ZrO_2 (Figures S4a,b). Based on these observations, palladium nanoparticles are also expected to be present on ternary systems, but a synergic interplay between the promoter, In_2O_3, and m-ZrO_2 most likely prevents additional sintering under reaction conditions, and consequent catalyst deactivation. Still, it is striking that the performance of $1Pd$-$5In_2O_3/m$-ZrO_2 does not deviate from that of $1Pd/5In_2O_3/m$-ZrO_2. In particular, because palladium is deposited onto In_2O_3/m-ZrO_2 rather than co-deposited with indium onto m-ZrO_2, and thus could interact less strongly with In_2O_3 (Figure 1a). This points to their active sites for methanol formation possessing similar structure, and hints at these materials undergoing surface reconstruction upon reaction, which must occur rapidly since no apparent induction time is observed (Figure 1a).

Reaction-Induced Catalyst Restructuring

Detailed space and time-resolved characterization were conducted to rationalize the highly selective and stable behavior of the ternary catalysts. EDX maps clearly evidenced palladium nanoparticles in fresh $1Pd$-$5In_2O_3/m$-ZrO_2 and $1Pd/5In_2O_3/m$-ZrO_2 (Figures 2a and S6a, respectively), whereas In_2O_3 is highly dispersed on the m-ZrO_2
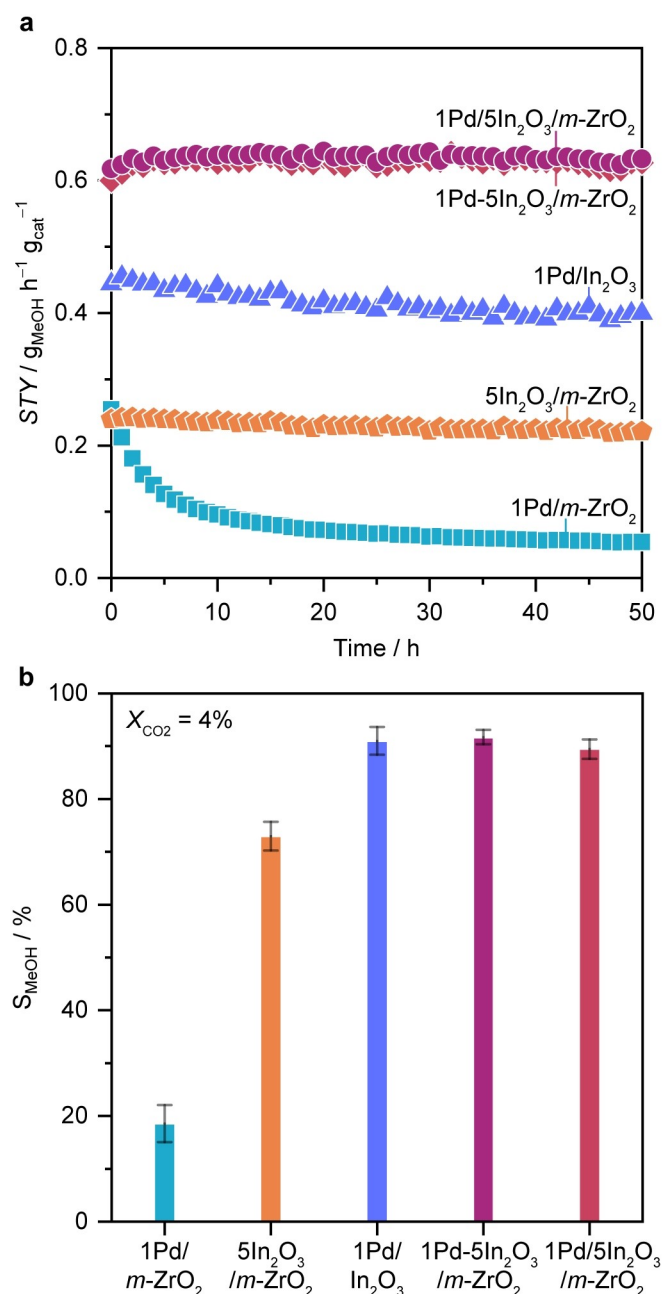
Figure 1. (a) Methanol space-time yield, *STY* and (b) selectivity, S_{MeOH} during CO_2 hydrogenation over ternary catalysts prepared by *one* (1Pd-5In$_2$O$_3$/*m*-ZrO$_2$) or *two-step* (1Pd/5In$_2$O$_3$/*m*-ZrO$_2$) impregnation, with binary systems serving as reference. S_{MeOH} was assessed at constant CO_2 conversion (*ca.* 4%) by adjusting the *GHSV* (24,000–96,000 cm^3 h^{-1} g$_{cat}^{-1}$), and corresponds to the averaged values measured over 50 h on stream with their corresponding error bars. Numbers preceding Pd or In$_2$O$_3$ in the catalyst codes indicate their nominal content in wt%. Reaction conditions: $T = 553$ K, $P = 5$ MPa, H$_2$/CO$_2 = 4$, and *GHSV* $= 24,000$ cm^3 h^{-1} g$_{cat}^{-1}$.

surface, particularly in the former sample, forming most likely monolayers. Remarkably, while no significant further agglomeration of palladium is detected in used samples collected after 50 h on stream (Figures 2b, S7, and S6b), we observe clear clustering of indium at the same location where palladium nanoparticles are present. This suggests a strong interaction between these phases and, more importantly, highlights that both ternary systems restructure and converge to a virtually identical architecture upon reaction, thereby explaining their very similar performance independent on the order of addition of the components (Figure 1a). For this reason, special emphasis was devoted to further investigate 1Pd-5In$_2$O$_3$/*m*-ZrO$_2$, which is attained by *one-step* impregnation. Accordingly, EDX mapping of the Pd–In particle shown in Figure 2c reveal that the concentration of palladium and indium varies heterogeneously within the particle regions (Figure 2d), suggesting a complex structure of different interacting phases. High-resolution high-angle annular dark-field STEM (HAADF-STEM) images support this claim as the morphology of the particles appear almost amorphous, while also often exhibiting a more crystalline core (Figure 2c).

Operando XAS experiments were conducted under pretreatment in He (1.5 MPa and from 303 to 553 K) and CO_2 hydrogenation conditions (1.5 MPa and 553 K) in the Pd and In *K*-edges to probe their corresponding local environments, while product evolution is evaluated by mass spectrometry (Figure S8). *Operando* XANES reveals that both palladium and indium exist as oxidized phases in the fresh catalyst (Figures 3a, b). Upon thermal treatment under He, however, a gradual reduction is observed for both elements; palladium fully reduces, matching the spectra of the reference material (1Pd/*m*-ZrO$_2$) comprising nanoparticles, while indium maintains partially reduced state (InO$_x$). Interestingly, exposure to the reaction mixture for 30 min causes significant changes to the palladium character and deviations with respect to the reference are observed (Figure 3a). This change indicates an interaction of palladium with indium that leads to alloy formation. Indium shows a further reduction, yet still maintaining characteristics of InO$_x$ phases. This is expected, based on microscopic analysis, as only a fraction of indium is expected to interact with palladium nanoparticles, while its majority is still highly dispersed on the *m*-ZrO$_2$ surface. This rapidly evolved architecture is preserved even after 12 h on stream (Figure 3a), accounting for the stable performance of the catalyst (Figure 1a).

In line with XANES spectra, EXAFS analysis of the fresh catalysts exhibits strong metal-oxygen (*M*-O) interactions for both 1Pd-5In$_2$O$_3$/*m*-ZrO$_2$ and Pd/*m*-ZrO$_2$ (Figure 3c). Under reaction conditions however, a clear difference is observed between the two catalysts. While Pd/*m*-ZrO$_2$ shows Pd–Pd contributions, the Pd–*M* contributions are clearly shifted for 1Pd-5In$_2$O$_3$/*m*-ZrO$_2$, which could be attributed to either alloying and/or palladium hydride (PdH$_x$) formation. However, no signal associated with hydrides is observed via H$_2$-TPR on used or activated 1Pd-5In$_2$O$_3$/*m*-ZrO$_2$ (Figure S9b) or bond elongation is evidenced by EXAFS, excluding PdH$_x$ formation (Table S5). Therefore, the changes in Pd–Pd/In distances are predominantly due to alloying between palladium and indium. Regarding the In *K*-edge EXAFS (Figure 3c), the sample largely exhibits In–O interactions and only a small In-*M* contribution is observed, which is shifted compared to that
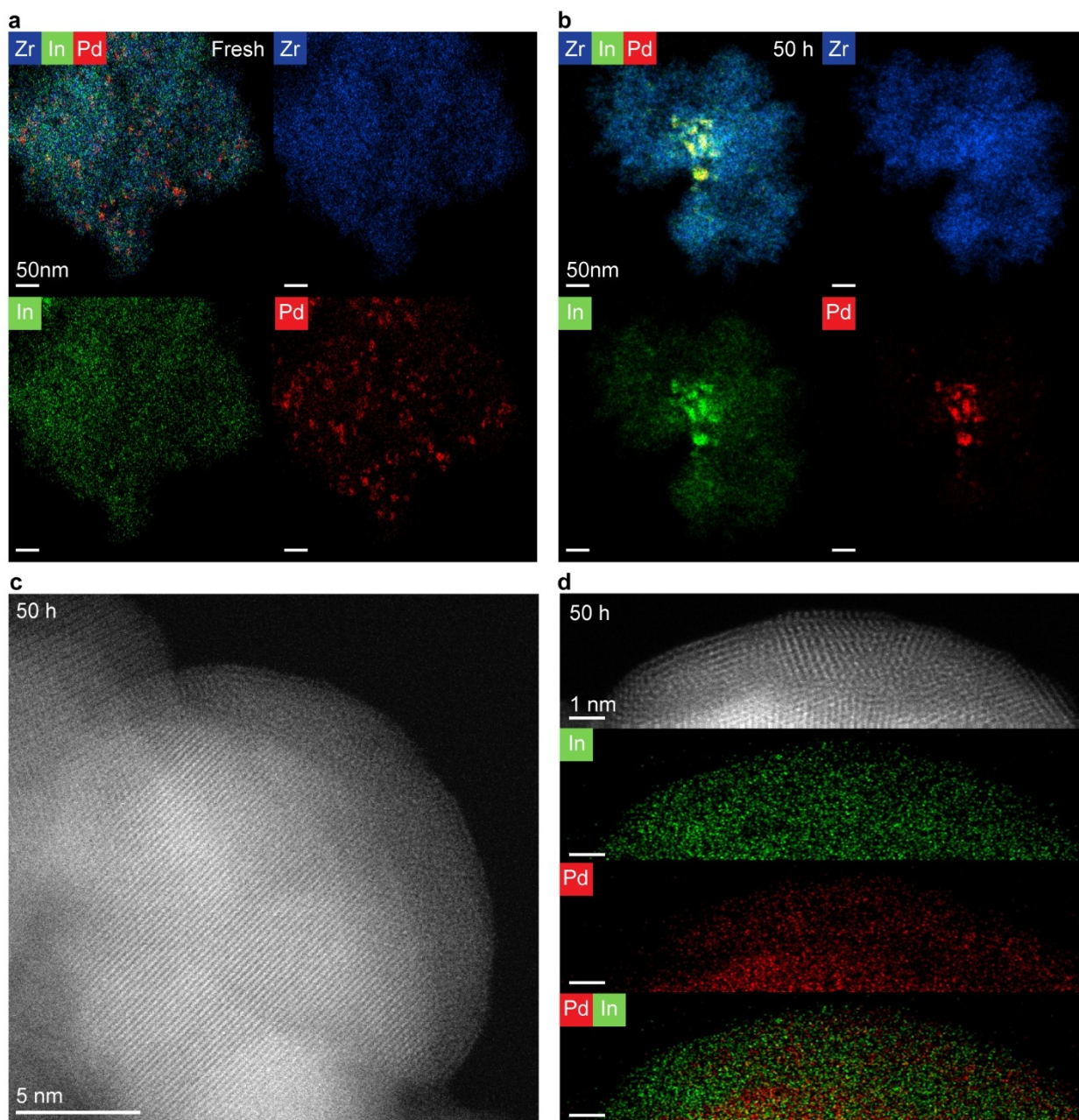
Figure 2. EDX maps of the 1Pd-5In$_2$O$_3$/m-ZrO$_2$ catalyst in (a) fresh form and (b) after CO$_2$ hydrogenation for 50 h. (c) STEM-HAADF image and (d) high magnification EDX maps of the 1Pd-5In$_2$O$_3$/m-ZrO$_2$ catalyst after CO$_2$ hydrogenation for 50 h. Reaction conditions: $T = 553$ K, $P = 5$ MPa, H$_2$/CO$_2 = 4$, and $GHSV = 24{,}000$ cm^3 h^{-1} g$_{cat}^{-1}$.

of the In foil. This can be rationalized on the premise that only a small fraction of indium is alloyed with palladium whereas its majority remains associated with *m*-ZrO$_2$. Further pieces of evidence regarding the alloy formation can be gathered by techniques that assess the chemical properties of these materials, such as their ability to bind CO or split H$_2$. Indeed, CO chemisorption experiments (Table S4) showed that a significantly lower amount of CO adsorbs on ternary catalysts, indicating a modified palladium surface.[10,27] This weakened interaction with CO has been reported for palladium alloys,[28] protecting their surfaces

from CO poisoning. In the case of 1Pd-5In$_2$O$_3$/*m*-ZrO$_2$, modification by indium results in the absence of peaks associated with PdH$_x$ (Figure S9). These observed changes, supported by standard characterization techniques (H$_2$-TPR, CO chemisorption and XAS), indicate significantly different properties between bare and modified palladium nanoparticles. These results explain the significant differences in methanol selectivity and *STY* between 1Pd-5In$_2$O$_3$/*m*-ZrO$_2$ and 1Pd/*m*-ZrO$_2$, (Figures 1a, b) as a consequence of palladium-indium alloy formation.
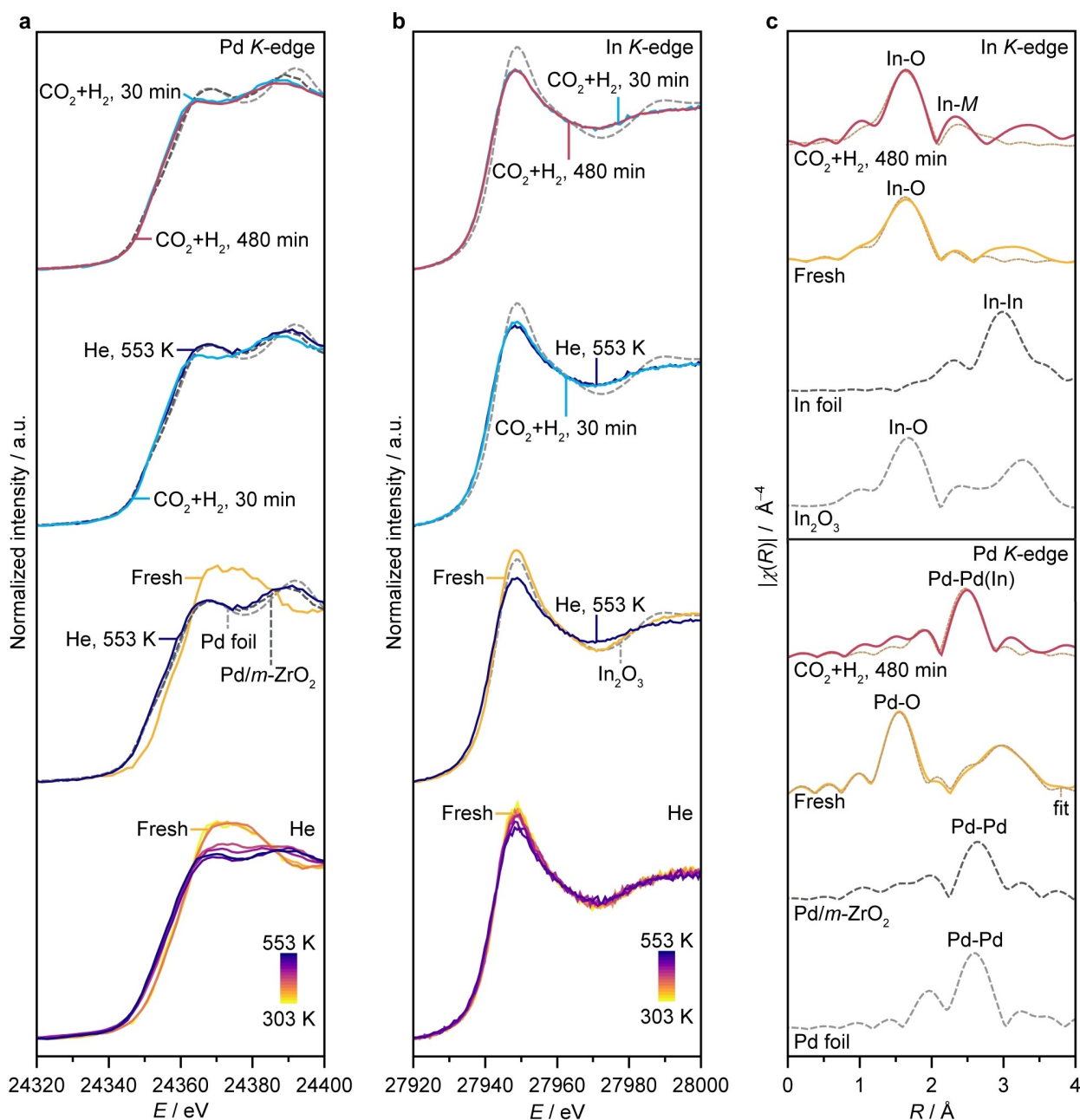
Figure 3. *Operando* (a) Pd and (b) In K-edge XANES spectra of 1Pd-5In$_2$O$_3$/m-ZrO$_2$ catalyst during the heating ramp (m_{cat} = 0.013 g, F_T = 15 cm^3 min^{-1}, heating rate = 5 K min^{-1}, T = 553 K, P = 1.5 MPa, and dwell time = 30 min in He) and under reaction conditions (m_{cat} = 0.013 g, F_T = 15 cm^3 min^{-1}, T = 553 K, P = 1.5 MPa, H$_2$/CO$_2$ = 4, dwell time = 480 min) with time on stream. (c) Fourier-transformed EXAFS spectra of 1Pd-5In$_2$O$_3$/m-ZrO$_2$ catalyst in fresh form and under reaction conditions corresponding to the spectra in **a** and **b**. XANES and EXAFS spectra of Pd and In foils, In$_2$O$_3$, and activated 1Pd/m-ZrO$_2$ (m_{cat} = 0.013 g, F_T = 15 cm^3 min^{-1}, T = 553 K, P = 1.5 MPa, H$_2$/CO$_2$ = 4, dwell time = 480 min) are shown as reference.

To shed light on the evolution of palladium-indium particles beyond the 5 nm range, a common limitation of XANES and EXAFS analyses,[21] we performed *operando* time-resolved XRD experiments. In principle, no characteristic signal of PdO and In$_2$O$_3$ phases can be detected in the fresh catalyst (Figure S10), due to their diffraction features overlapping with that of the m-ZrO$_2$ carrier and high dispersion of indium, respectively, in line with microscopy

findings (Figure 2a). While XANES (Figures 3a,b) showed that palladium and, to a lesser extent, indium already reduce upon heating of the catalyst in He, no apparent structural changes are observed by XRD (Figures 4a,b). Since the main diffraction lines of metallic palladium and InPd$_x$ phases do not overlap with that of m-ZrO$_2$, this indicates that reduced palladium and indium species generated at this stage do not form nanostructures with long-range crystal-

linity, and therefore remain XRD silent. In contrast, diffraction peaks at 6.26 and 6.36° 2θ specific to $InPd_2$ alloys appeared with progressing exposure of the catalyst to the CO_2/H_2 mixture at 553 K (Figures 4a,b). This confirms that the formation of $InPd_2$ nanoparticles occurs under reductive environments. Interestingly, a close look at the reflections at 6.26 and 6.36° 2θ (Figure 4b) revealed that their intensity and width stop evolving within *ca.* 30 min. It is noteworthy that even anisotropic broadening of the reflections caused by further changes in shape and size of the particles can be easily detected by synchrotron XRD due to its high sensitivity.[22] Hence, these findings are strong evidence that the restructuring process of the ternary catalysts occurs rapidly, equilibrating before the first performance data is analyzed by gas chromatography (*ca.* 30 min), which explains their stable methanol *STY* (Figure 1a) with no apparent induction time.

In addition to the formation of crystalline $InPd_2$ nanoparticles confirmed by *operando* HR-XRD, high-resolution STEM-EDX indicates that small (sub)nanometer domains with low degree of ordering are present at the surface of these nanostructures (Figure 2d). Nonetheless, the EDX signal is inherently weak due to detection limitations and thus susceptible to noise by, *e.g.* spurious X-rays, especially at high magnification and low electron beam current. Therefore, the used catalyst retrieved after 50 h on stream was further investigated by a combination of HAADF-STEM and electron energy-loss spectroscopy (EELS, Figures 5a,c and S11). The latter is well known for its high sensitivity to probe surface changes in atomic structure and chemical properties at metal-oxide interfaces in heterogeneous catalysts.[29–36] The EELS maps clearly reveal that the mixed palladium-indium nanoparticles possess a core–shell-like structure (Figures 5c, and S11). Analyzing the corresponding HR-STEM image reveals that the palladium-rich areas overlap well with the crystalline core-regions. By inspecting the EELS spectra in different areas of the particles (Figure 5f and S11), we observe that the Pd-$M_{5,4}$ peak disappears in the amorphous shells (Figure 5d,e), suggesting only trace-amounts of palladium in the shell. Together with STEM-EDX and *operando* XRD and XAS findings (Figures 2a, 3a–c, 4a, 4b, and 5b), these results strongly suggest that In_2O_3 migrates onto palladium particles upon reaction, forming crystalline $InPd_x$ nanostructures in the core that are encapsulated to some extent by amorphous layers comprising partially reduced indium oxide species (InO_x), as illustrated in Figure 5g. Furthermore, *operando* and *ex situ* characterization point to the alloying process being irreversible under reaction and even after exposure to air, underlining the stability of the $InPd_x$ phase.

With detailed experimental investigations evidencing the reaction-induced restructuring of the ternary systems, we sought to further rationalize this process by DFT simulations using a thermodynamic model. To illustrate the driving force for the restructuring, we computed the interaction energy (E_{int}) between an $In_2O_3(111)$ monolayer at different degrees of reduction with both m-ZrO_2 (-111) and metallic Pd(111) surfaces (Figure S14, see detailed description in the Experimental Section, Supporting Information). At low degrees of
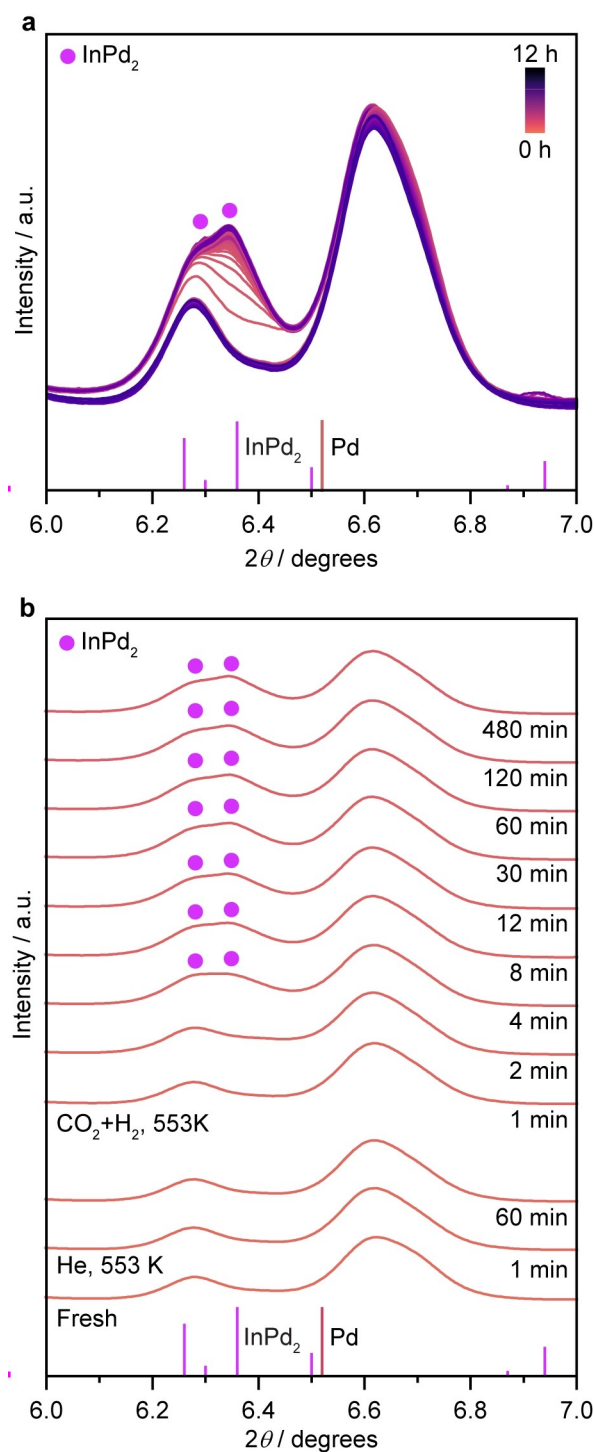

Figure 4. *Operando* time-resolved HR-XRD patterns of 1Pd-5In$_2$O$_3$/m-ZrO$_2$ catalyst during the heating ramp (m_{cat} = 0.013 g, F_T = 15 cm^3 min^{-1}, heating rate = 5 K min^{-1}, T = 553 K, P = 1.5 MPa, and dwell time = 30 min in He) and under reaction conditions (m_{cat} = 0.013 g, F_T = 15 cm^3 min^{-1}, T = 553 K, P = 1.5 MPa, H$_2$/CO$_2$ = 4, dwell time = 480 min) with (**a**) continuous and (**b**) selected time on stream. Diffractograms were acquired every 30 s using monochromatic light (λ = 0.25509 Å). Vertical lines show reference data (InPd$_2$, ICSD ID 417907).
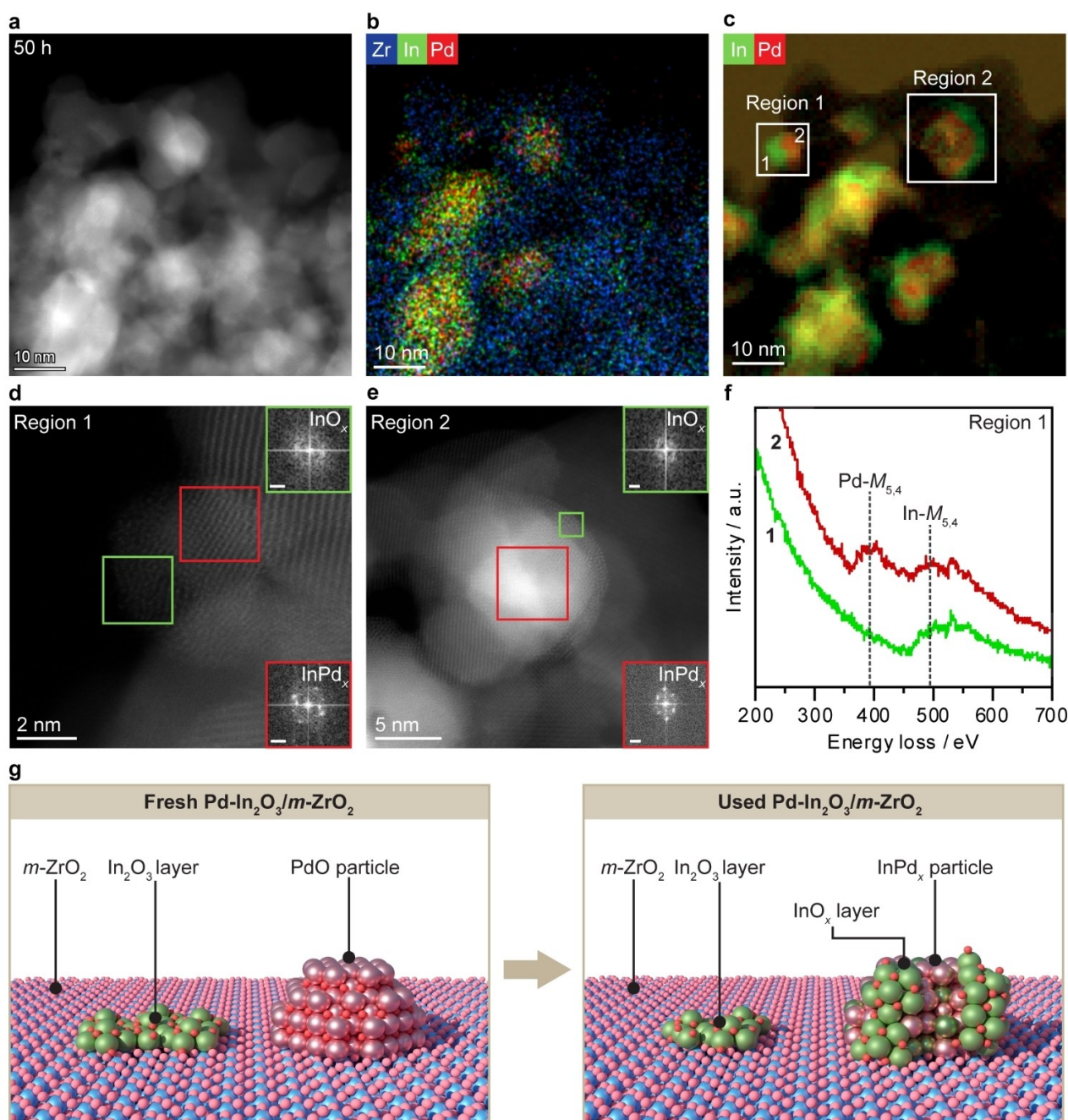
Figure 5. (a) HAADF-STEM image with corresponding (b) EDX and (c) EELS maps of 1Pd-5In$_2$O$_3$/m-ZrO$_2$ catalyst after CO$_2$ hydrogenation for 50 h. (d, e) High magnification STEM images of regions 1 and 2 shown in (c). Insets in (d, e) show fast Fourier transforms of indicated areas, evidencing the presence of both amorphous InO$_x$ and crystalline InPd$_x$ phases. (f) Averaged EELS spectra of the green (green curve) and red (red curve) regions shown in d. The palladium peak clearly disappears in the amorphous shell. (g) Schematic representation of the catalyst architecture of fresh and used 1Pd-5In$_2$O$_3$/m-ZrO$_2$ catalyst, depicted on the left and right, respectively. Reaction conditions: $T=553$ K, $P=5$ MPa, H$_2$/CO$_2=4$, and GHSV $=24,000$ cm^3 h^{-1} g$_{cat}^{-1}$.

reduction (*i.e.*, 0–17% oxygen loss), In$_2$O$_3$ interacts similarly with the two surfaces (Figure S14). This agrees with the high expected dispersion of this phase over m-ZrO$_2$ in fresh catalysts, as evidenced by microscopy analyses (Figure 2a). For high degrees of reduction (*i.e.*, >17%, Figure S14), InO$_x$ prefers to interact with metallic palladium compared to m-ZrO$_2$. As more O atoms are removed from In$_2$O$_3$, its surface

energy increases translating into a less favorable wetting of the m-ZrO$_2$ carrier, and thus higher mobility, as previously reported for In$_2$O$_3$/m-ZrO$_2$ catalysts under CO$_2$ hydrogenation conditions.[24] Consequently, because oxygen vacancy formation on In$_2$O$_3$ is fostered by thermal treatments in both inert and reductive atmospheres,[1,17] the migration and stabilization of InO$_x$ overlayers onto metallic palladium

nanoparticles experimentally evidenced for Pd-In$_2$O$_3$/m-ZrO$_2$ catalysts is driven by these thermodynamic considerations. Interestingly, this suggests that these systems experience a special case of strong metal-support interactions (SMSI) under reaction conditions. Generally, SMSI overlayer formation on metal particles is reported for binary systems, where In$_2$O$_3$ and other reducible oxides serve as supports.[32,34,37–39] For ternary Pd-In$_2$O$_3$/m-ZrO$_2$ systems, however, the active InO$_x$ phase rather than the m-ZrO$_2$ support partially encapsulates the particles of the palladium promoter, which we attribute to its more strongly reducible nature rendering it more mobile under reaction conditions. The reduction of In$_2$O$_3$ is corroborated experimentally, by linear fitting combination (LFC) analysis of spectra shown in Figure 3b using In$_2$O$_3$ and In foil as the reference materials, which indicates that In$_2$O$_3$ is reduced by *ca.* 35 % under reaction conditions. Finally, because indium and palladium are not mixed in the fresh catalyst, we put forward that the restructuring of Pd-In$_2$O$_3$/m-ZrO$_2$ catalysts begins with migration of InO$_x$ onto palladium nanoparticles, followed by alloy formation between part of the oxidic phase and palladium (Figure 5g). Indeed, the computed formation energies of InPd$_2$ and InPd (-1.51 and -0.97 eV, respectively) indicate a high tendency for the formation InPd$_x$ alloy phases, in line with *operando* XAS and XRD results (Figures 3a and 4a,b).

Mapping Catalyst Structure to Function

CO$_2$ hydrogenation to methanol requires the activation of the reactants (CO$_2$ and H$_2$), followed by hydride-proton transfers avoiding the RWGS side reaction, which leads to CO poisoning (Figure S15). For a given catalytic material to be effective in catalyzing this transformation, a combination of acid-base properties (to trap CO$_2$) and easy activation of H$_2$ is needed. In general, metallic centers show poor CO$_2$ activation properties whereas basic centers on oxides (lattice oxygen atoms) uptake CO$_2$ effectively. However, oxides possess a limited ability to split H$_2$, as this process takes place *via* a heterolytic route generating protons (H$^+$) and hydrides (H$^-$). In contrast, this can be easily solved by metals since they homolytically activate H$_2$ in low-energy processes.[5,40] To assess the role of the distinct catalytic components in the reaction, various model surfaces were considered based on the experimentally revealed catalyst architecture (see **Modelling of the Catalytic Systems** subsection, Supporting Information). It is worth noting that adsorption studies conducted in ultra-high vacuum do not fully capture the catalyst structure under real operating conditions due to the pressure and associated material gap.[41–43] Therefore, we computed adsorption energies (E_{ads}) of CO$_2$, dissociated H$_2$, and CO on these experimentally-guided model surfaces (see Experimental Section in the Supporting Information).This holistic approach enabled us to bridge the pressure gap, and provides valuable insights to rationalize the catalytic activity and stability of Pd-In$_2$O$_3$/m-ZrO$_2$ systems. Figure 6 shows the most relevant and favorable E_{ads}, while the values associated with different

adsorption conformations and models can be found in Figures S16–17. CO$_2$ adsorption is favored on m-ZrO$_2$ and In$_2$O$_3$ over Pd, while the opposite trend is observed for H$_2$ dissociation products. These results indicate that in binary catalysts (Pd/In$_2$O$_3$, Pd/m-ZrO$_2$), CO$_2$ is activated and hydrogenated on the metal oxides and H$_2$ splitting takes places on Pd (Figure S15). This implies spillover of hydrogen from Pd to the metal oxides, which although it can be long-range, it is an stochastic process and thus ineffective.[44,45] In addition, the ability of palladium surfaces to activate H$_2$ (as H atoms) boosts both methanol and carbon monoxide formation. On the contrary, the computed $E_{ads,CO}$ on InPd$_2$ and InPd (Figure S16) points to CO adsorption being weakened with respect to extended Pd surfaces. This contributes to the ternary catalysts circumventing CO poisoning and controlling the H coverage, which can explain the CO chemisorption and catalytic tests (Table S4 and Figure 1a,b).

For the restructured Pd-In$_2$O$_3$/m-ZrO$_2$, InO$_x$ overlayers permit an easy CO$_2$ adsorption at the basic sites on the edge of In$_4$O$_5$ clusters deposited on Pd and InPd$_2$ surfaces (In$_4$O$_5$-Pd and In$_4$O$_5$-InPd$_2$ models, Figure S16). Concomitantly, H$_2$ can be homolytically activated in the InPd$_2$ regions nearby the InO$_x$ clusters allowing the formation of InO$_x$H and InPd$_2$H species at the interface ($\Delta E = -0.89$ eV). This configuration promotes selective CO$_2$ hydrogenation to methanol by minimizing transport as all active species are confined in close proximity. Overall, the interface between InO$_x$ clusters and Pd/InPd$_x$ nanoparticles are the active sites for CO$_2$ hydrogenation to methanol on the ternary Pd-In$_2$O$_3$/ZrO$_2$ system (Figure 6). It should be noted however that indium phases that do not associate with palladium but rather remain dispersed on ZrO$_2$ still contribute to the overall activity, considering the reactivity of In$_2$O$_3$/m-ZrO$_2$.

Our study reveals a remarkable result that two distinct synthetic methods - the wet chemical synthesis employed here and the FSP method demonstrated previously[17] - can produce ternary systems with similarly stable and selective behavior, despite exhibiting very different architectures. The essential functions of the catalysts include (i) facilitating reactant activation via acid-base or metal catalysis, (ii) efficiently removing the desired product through acid-base catalysis, and (iii) enabling convenient transport of activated reactants. In the systems prepared by impregnation, the active site is formed by the migration of small InO$_x$ clusters to the metal surface under reducing conditions, incorporating some of the In atoms as an alloy. Comparatively, the FSP method creates low-nuclearity Pd clusters with sufficient metallic character, surrounded by the In$_2$O$_3$ oxide matrix to form the active ensemble (Figure S18). Similar structural characteristics were also observed for Pd-In$_2$O$_3$ obtained by coprecipitation.[5] However, the current study demonstrates a more practical and scalable catalyst with optimal indium content, while achieving similar methanol *STY* and stability. Our work highlights that different active site configurations can perform similar functions and the fact that these structures may appear under reaction conditions. Moreover, our novel architecture obtained using a common synthesis method demonstrates the potential for improving methanol synthesis with high selectivity.
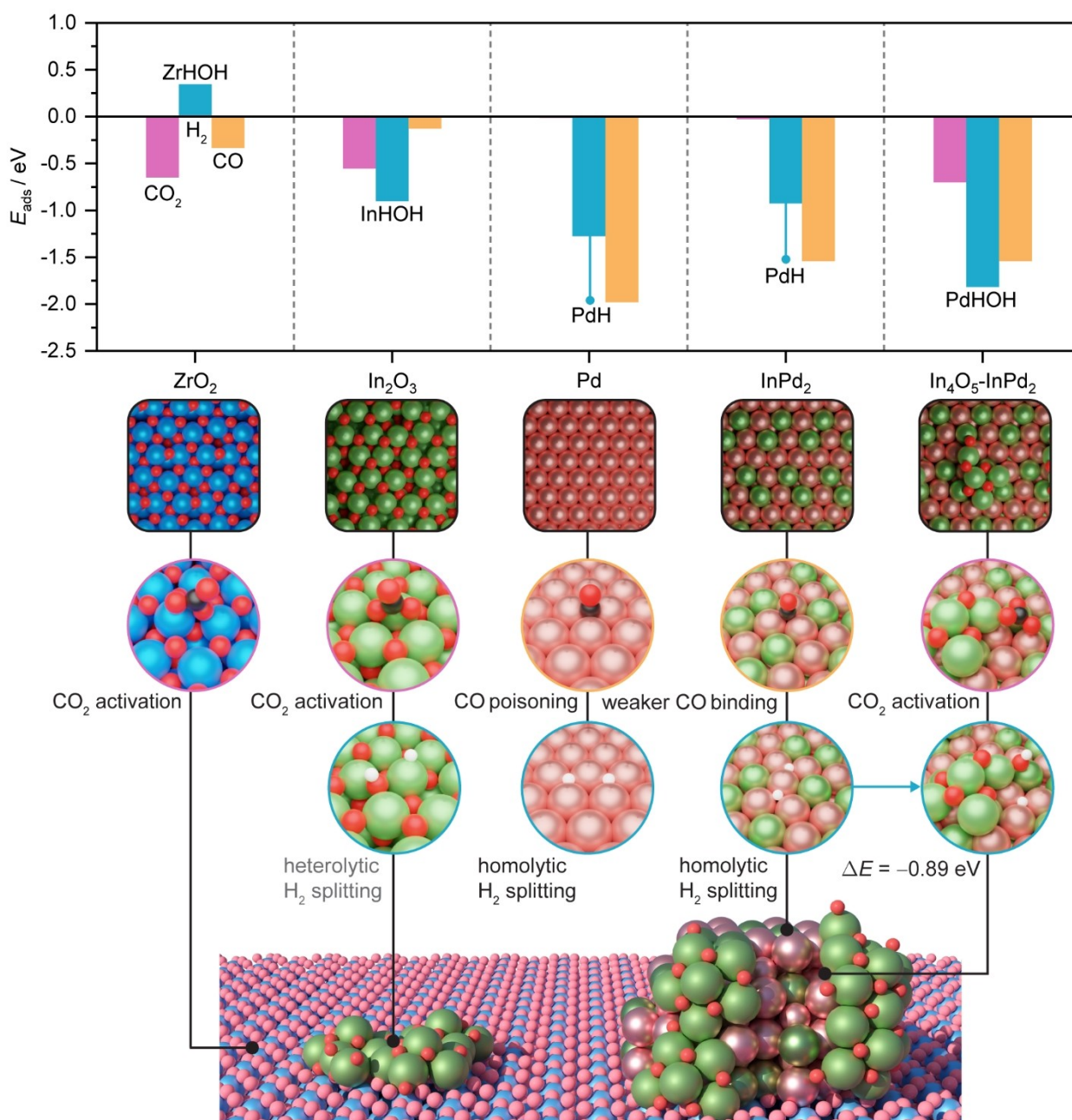
Figure 6. Adsorption energies, E_{ads}, of reaction species on relevant surfaces representative of the different constituents of ternary Pd-In_2O_3/m-ZrO_2 systems attained by impregnation. The adsorption mode for the dissociated hydrogen is indicated for each model. Snapshots of activated CO_2 and H_2 indicate the locations at which these key steps for methanol synthesis are more favored over the catalyst surface. The formation of InO_xH and $InPd_2H$ species is favored on In_4O_5-$InPd_2$ after barrierless homolytic H_2 splitting on $InPd_2$. Snapshots of CO specify surfaces at which poisoning by this specie is favored. Color code of DFT models: Zr (blue), In (green), Pd (light pink), O (red), C (dark gray), and H (white).

Conclusion

This study demonstrates that ternary Pd-In_2O_3/m-ZrO_2 catalysts produced by scalable wet impregnation routes undergo rapid surface reconstruction during CO_2 hydrogenation. Irrespective of the order of addition of the Pd and In precursors during the synthesis, this results in a stable and selective catalyst architecture with improved methanol productivity compared to binary systems. *Operando* XAS

confirms the autoreduction of palladium nanoparticles to a metallic state prior to reaction, and the partial reduction of In_2O_3 into InO_x species that migrate onto the metallic palladium surface. EELS and *operando* HR-XRD analyses reveal that the catalysts further restructure into $InPd_x$ alloy particles partially encapsulated by InO_x layers induced by the reductive environment during CO_2 hydrogenation. DFT simulations support that metal-metal oxide interactions govern the structural evolution and reactivity. The $InPd_x$

phase activates H_2 homolytically, while the InO_x overlayer facilitates acid-base steps, enhancing methanol formation. Overall, our study advances the understanding of reaction-induced structural dynamics in In_2O_3-based catalytic systems and uncovers a highly effective architecture for CO_2-based methanol synthesis. It also highlights the potential for surface reconstruction to tailor other reducible oxides in heterogeneous catalysis.

Supporting Information

Supporting Information is available from the Wiley Online Library or from the author.

Acknowledgements

Conflict of Interest

The authors declare no conflict of interest.

Data Availability Statement

The data that support the findings of this study are openly available in Zenodo at https://doi.org/10.5281/zenodo.7916390.[46] DFT data can be found online in the ioChem-BD repository,[47,48] at https://doi.org/10.19061/iochem-bd-1-275.

Keywords: CO_2 Hydrogenation · Metal-Metal Oxide Interactions · Methanol Synthesis · *Operando* Analysis · Pd-In_2O_3/ZrO_2 Catalyst

[1] O. Martin, A. J. Martín, C. Mondelli, S. Mitchell, T. F. Segawa, R. Hauert, C. Drouilly, D. Curulla-Ferré, J. Pérez-Ramírez, *Angew. Chem. Int. Ed.* **2016**, *55*, 6261–6265.

[2] A. González-Garay, M. S. Frei, A. Al-Qahtani, C. Mondelli, G. Guillén-Gosálbez, J. Pérez-Ramírez, *Energy Environ. Sci.* **2019**, *12*, 3425–3436.

[3] G. A. Olah, *Angew. Chem. Int. Ed.* **2005**, *44*, 2636–2639.

[4] M. S. Frei, M. Capdevila-Cortada, R. García-Muelas, C. Mondelli, N. López, J. A. Stewart, D. Curulla Ferré, J. Pérez-Ramírez, *J. Catal.* **2018**, *361*, 313–321.

[5] M. S. Frei, C. Mondelli, R. García-Muelas, K. S. Kley, B. Puértolas, N. López, O. V. Safonova, J. A. Stewart, D. Curulla Ferré, J. Pérez-Ramírez, *Nat. Commun.* **2019**, *10*, 3377.

[6] S. Dang, B. Qin, Y. Yang, H. Wang, J. Cai, Y. Han, S. Li, P. Gao, Y. Sun, *Sci. Adv.* **2020**, *6*, eaaz2060.

[7] J. Ye, Q. Ge, C. J. Liu, *Chem. Eng. Sci.* **2015**, *135*, 193–201.

[8] T. Pinheiro Araújo, J. Morales-Vidal, T. Zou, R. García-Muelas, P. O. Willi, K. M. Engel, O. V. Safonova, D. Faust Akl, F. Krumeich, R. N. Grass, et al., *Adv. Energy Mater.* **2022**, *12*, 2103707.

[9] T. Y. Chen, C. Cao, T. B. Chen, X. Ding, H. Huang, L. Shen, X. Cao, M. Zhu, J. Xu, J. Gao, et al., *ACS Catal.* **2019**, *9*, 8785–8797.

[10] J. L. Snider, V. Streibel, M. A. Hubert, T. S. Choksi, E. Valle, D. C. Upham, J. Schumann, M. S. Duyar, A. Gallo, F. Abild-Pedersen, et al., *ACS Catal.* **2019**, *9*, 3399–3412.

[11] N. Rui, Z. Wang, K. Sun, J. Ye, Q. Ge, C. jun Liu, *Appl. Catal. B* **2017**, *218*, 488–497.

[12] Z. Han, C. Tang, J. Wang, L. Li, C. Li, *J. Catal.* **2021**, *394*, 236–244.

[13] M. S. Frei, C. Mondelli, A. Cesarini, F. Krumeich, R. Hauert, J. A. Stewart, D. Curulla Ferré, J. Pérez-Ramírez, *ACS Catal.* **2020**, *10*, 1133–1145.

[14] C. Yang, C. Pei, R. Luo, S. Liu, Y. Wang, Z. Wang, Z. J. Zhao, J. Gong, *J. Am. Chem. Soc.* **2020**, *142*, 19523–19531.

[15] N. Rui, F. Zhang, K. Sun, Z. Liu, W. Xu, E. Stavitski, S. D. Senanayake, J. A. Rodriguez, C.-J. Liu, *ACS Catal.* **2020**, *10*, 11307–11317.

[16] A. Tsoukalou, P. M. Abdala, A. Armutlulu, E. Willinger, A. Fedorov, C. R. Müller, *ACS Catal.* **2020**, *10*, 10060–10067.

[17] T. Pinheiro Araújo, C. Mondelli, M. Agrachev, T. Zou, P. O. Willi, K. M. Engel, R. N. Grass, W. J. Stark, O. V. Safonova, G. Jeschke, et al., *Nat. Commun.* **2022**, *13*, 5610.

[18] S. Pokhrel, L. Mädler, *Energy Fuels* **2020**, *34*, 13209–13224.

[19] S. Ding, H. A. Chen, O. Mekasuwandumrong, M. J. Hülsey, X. Fu, Q. He, J. Panpranot, C. M. Yang, N. Yan, *Appl. Catal. B* **2021**, *281*, 119471.

[20] R. Koirala, S. E. Pratsinis, A. Baiker, *Chem. Soc. Rev.* **2016**, *45*, 3053.

[21] A. Beck, M. A. Newton, M. Zabilskiy, P. Rzepka, M. G. Willinger, J. A. van Bokhoven, *Angew. Chem. Int. Ed.* **2022**, *61*, e202200301.

[22] O. Martin, C. Mondelli, A. Cervellino, D. Ferri, D. Curulla-Ferré, J. Pérez-Ramírez, *Angew. Chem. Int. Ed.* **2016**, *55*, 11031–11036.

[23] A. Tsoukalou, P. M. Abdala, D. Stoian, X. Huang, M. G. Willinger, A. Fedorov, C. R. Müller, *J. Am. Chem. Soc.* **2019**, *141*, 13497–13505.

[24] X. Zhang, A. V. Kirilin, S. Rozeveld, J. H. Kang, G. Pollefeyt, D. F. Yancey, A. Chojecki, B. Vanchura, M. Blum, *ACS Catal.* **2022**, *12*, 3868–3880.

[25] A. Baiker, D. Gasser, *J. Chem. Soc. Faraday Trans. 1* **1989**, *85*, 999–1007.

[26] Y.-P. Du, A. M. Bahmanpour, L. Milošević, F. Héroguel, M. D. Mensi, O. Kröcher, J. S. Luterbacher, *ACS Catal.* **2020**, *10*, 12058–12070.

[27] Z. Wu, E. C. Wegener, H.-T. Tseng, J. R. Gallagher, J. W. Harris, R. E. Diaz, Y. Ren, F. H. Ribeiro, J. T. Miller, *Catal. Sci. Technol.* **2016**, *6*, 6965–6976.

[28] M. T. Darby, E. C. H. Sykes, A. Michaelides, M. Stamatakis, *Top. Catal.* **2018**, *61*, 428–438.

[29] R. F. Klie, M. M. Disko, N. D. Browning, *J. Catal.* **2002**, *205*, 1–6.

[30] W. Zhou, I. E. Wachs, C. J. Kiely, *Curr. Opin. Solid State Mater. Sci.* **2012**, *16*, 10–22.

[31] S. Chenna, P. A. Crozier, *ACS Catal.* **2012**, *2*, 2395–2402.

[32] Y. Niu, X. Liu, Y. Wang, S. Zhou, Z. Lv, L. Zhang, W. Shi, Y. Li, W. Zhang, D. S. Su, B. Zhang, *Angew. Chem. Int. Ed.* **2019**, *131*, 4276–4281.

[33] X. Huang, D. Teschner, M. Dimitrakopoulou, A. Fedorov, B. Frank, R. Kraehnert, F. Rosowski, H. Kaiser, S. Schunk, C. Kuretschka, R. Schlogl, M.-G. Willinger, A. Trunschke, *Angew. Chem. Int. Ed.* **2019**, *58*, 8709–8713.

[34] T. Pu, W. Zhang, M. Zhu, *Angew. Chem. Int. Ed.* **2023**, *62*, e202212278.

[35] Y. Zhang, J. Liu, K. Qian, A. Jia, D. Li, L. Shi, J. Hu, J. Zhu, W. Huang, *Angew. Chem. Int. Ed.* **2021**, *60*, 12074–12081.

[36] A. Ruiz Caridad, R. Erni, A. Vogel, M. D. Rossell, *Micron* **2022**, *160*, 103331.

[37] N. Rui, X. Wang, K. Deng, J. Moncada, R. Rosales, F. Zhang, W. Xu, I. Waluyo, A. Hunt, E. Stavitski, et al., *ACS Catal.* **2023**, *13*, 3187–3200.

[38] J. C. Matsubu, S. Zhang, L. DeRita, N. S. Marinkovic, J. G. Chen, G. W. Graham, X. Pan, P. Christopher, *Nat. Chem.* **2017**, *9*, 120–127.

[39] K. J. Sawant, Z. Zeng, J. P. Greeley, *Chem. Sci.* **2023**, *14*, 3206–3214.

[40] M. S. Frei, C. Mondelli, R. García-Muelas, J. Morales-Vidal, M. Philipp, O. V. Safonova, N. López, J. A. Stewart, D. Curulla Ferré, J. Pérez-Ramírez, *Nat. Commun.* **2021**, *12*, 1960.

[41] A. Urakawa, *Nat. Catal.* **2021**, *4*, 447–448.

[42] A. Beck, M. Zabilskiy, M. A. Newton, O. Safonova, M. G. Willinger, J. A. van Bokhoven, *Nat. Catal.* **2021**, *4*, 488–497.

[43] N. J. Divins, D. Kordus, J. Timoshenko, I. Sinev, I. Zegkinoglou, A. Bergmann, S. W. Chee, S. Widrinna, O. Karslıoğlu, H. Mistry, M. Lopez Luna, J. Qiang Zhong, A. S. Hoffman, A. Boubnov, J. Anibal Boscoboinik, M. Heggen, R. E. Dunin-Borkowski, S. R. Bare, B. Roldan Cuenya, *Nat. Commun.* **2021**, *12*, 1435.

[44] R. Prins, *Chem. Rev.* **2012**, *112*, 2714–2738.

[45] T. Kamada, T. Ueda, S. Fukuura, T. Yumura, S. Hosokawa, T. Tanaka, D. Kan, Y. Shimakawa, *J. Am. Chem. Soc.* **2023**, *145*, 1631–1637.

[46] T. Pinheiro Araújo, J. Morales-Vidal, G. Giannakakis, C. Mondelli, H. Eliasson, R. Erni, J. A. Stewart, S. Mitchell, N. López, J. Pérez-Ramírez, *Zenodo* **2022**, https://doi.org/10.5281/zenodo.7916390.

[47] M. Álvarez-Moreno, C. de Graaf, N. López, F. Maseras, J. M. Poblet, C. Bo, *J. Chem. Inf. Model.* **2015**, *55*, 95–103.

[48] C. Bo, F. Maseras, N. López, *Nat. Catal.* **2018**, *1*, 809–810.